

# Two-Dimensional Modelling of Optical HST and Infrared Tip-Tilt Images of Quasar Host Galaxies

R.J. McLure<sup>1,2</sup>, J.S. Dunlop<sup>1</sup>, M. J. Kukula<sup>1</sup>

<sup>1</sup>*Institute for Astronomy, University of Edinburgh, Blackford Hill, Edinburgh, EH9 3HJ*

<sup>2</sup>*Nuclear and Astrophysics Laboratory, University of Oxford, Keble Road, Oxford, OX1 3RH*

Accepted for publication in MNRAS

## ABSTRACT

A description is given of the method used to extract quasar host-galaxy parameters from the deep Hubble Space Telescope (HST) quasar images presented by McLure et al. (1999) and Dunlop et al. (2000). We then give the results of extensive testing of this technique on a wide range of simulated quasar+host combinations spanning the redshift range of our HST study ( $0.1 < z < 0.3$ ). These simulations demonstrate that, when applied to our deep HST images, our method of analysis can easily distinguish the morphological type of a given host galaxy, as well as determining its scalelength, luminosity, axial ratio and position angle to within an accuracy of a few percent. We also present new infrared tip-tilt images of 4 of the most luminous quasars in our HST sample, along with the outcome of modelling these data in a similar manner. The results provide further confidence in the accuracy of the derived host-galaxy scalelengths, and allow accurate determination of  $R - K$  colours for this subset of sources. All 4 of these quasar host galaxies have very similar red colours,  $R - K = 2.9 \pm 0.2$ , indicative of a well-evolved stellar population.

**Key words:** galaxies: active – galaxies: photometry – infrared: galaxies – quasars: general

## 1 INTRODUCTION

In two companion papers (McLure et al. 1999; Dunlop et al. 2000) we present initial and final results from a deep Hubble Space Telescope (HST) imaging survey of radio-quiet quasars (RQs), radio-loud quasars (RLQs) and radio galaxies (RGs). The results presented in these papers were derived from the HST images using a two-dimensional modelling technique developed to cope with such complications as central image saturation, the undersampled nature of Wide Field (WF) camera images, accurate image centering, and the precise form of the HST point spread function (PSF). The primary purpose of this paper is to provide a description of this image analysis method, and to present the results of extensive testing on simulated active-nucleus+host-galaxy images constructed to span the full range of parameter space, and to mimic as closely as possible the real HST data. These tests on simulated data were central to the development of our modelling technique, and also provide a means of estimating the typical errors in the derived host galaxy parameters as a function of redshift.

We also present new data in the form of infrared tip-tilt images of 4 of the most luminous quasars in our HST-imaging sample, and give the results of applying our two-dimensional modelling technique to these new  $K$ -band data. The results

provide further confidence in our analysis technique, and allow us to determine accurate  $R - K$  colours for the hosts of these 4 quasars.

The layout of the paper is as follows. In section 2 we briefly review the main modelling algorithm (for details see Taylor et al. 1996), and explain how the various problems which are specific to deep HST imaging were tackled. In section 3 we explain how synthetic HST quasar+host images were constructed to allow tests of the ability of the modelling technique to reclaim reliable host-galaxy parameters as a function of redshift and nuclear:host ratio. We then present the results of these tests before proceeding in sections 4 and 5 to describe extensions to the modelling algorithm which were introduced to avoid having to make the assumption that the host galaxies were either perfect deVaucouleurs spheroids, or Freeman discs. The new UKIRT Tip-Tilt IRCAM3 images of a subset of the quasar sample are presented in section 6 along with the results of modelling these data in a manner basically identical to that used to model the HST data. We then briefly describe the outcome of comparing the UKIRT- and HST-derived galaxy parameters for these objects, before summarizing our main conclusions in section 7.

## 2 TWO-DIMENSIONAL MODELLING OF QUASAR HOST GALAXIES

Given the difficulties associated with one-dimensional analysis techniques it was decided that a fully two-dimensional approach was needed to fully exploit the depth and resolution of the new HST and UKIRT host-galaxy data. The two-dimensional modelling code used in the analysis described in this paper, McLure et al. (1999) and Dunlop et al. (2000), is a development of that which was originally designed for the analysis of the IRCAM 1 *K*-band imaging of this sample (Dunlop et al. 1993, Taylor et al. 1996). Consequently, only a brief outline of the general algorithm is supplied here, with those interested in a detailed description being referred to Taylor et al. (1996).

The model host galaxies are initially constructed on a two-dimensional array with the surface-brightness of each pixel described by either a de Vaucouleurs  $r^{1/4}$  law (de Vaucouleurs & Capaccioli 1979):

$$\mu(r) = \mu_o \exp \left[ -7.67 \left( \left( \frac{r}{r_e} \right)^{1/4} - 1 \right) \right] \quad (1)$$

or a Freeman disc law (Freeman 1970):

$$\mu(r) = \mu_o \exp \left( -\frac{r}{r_o} \right) \quad (2)$$

The model galaxies are constructed at much higher resolution than the data plate-scale in order to accurately simulate the rapidly varying surface brightness at small radii (particularly important with the  $r^{1/4}$  profile). Following re-sampling of the model host galaxies, an arbitrarily large amount of flux is added to the central pixel to represent the unresolved nuclear contribution. In order to produce a simulated observation this ‘zero-seeing’ model is then convolved with a high signal-to-noise observation of the instrumental point spread function (PSF). The goodness of fit between this convolved model and the actual data is then tested on a pixel-by-pixel basis via the  $\chi^2$  statistic, with the parameters determining the form of the model being iterated to find the minimum  $\chi^2$  solution. The model parameters which are left free during this minimization process are:

- The luminosity of the nucleus
- The central brightness of the host galaxy
- The scalelength of the host galaxy
- The position angle of the host galaxy
- The axial ratio of the host galaxy

### 2.1 The WFPC2 PSF

Many authors who have investigated host galaxies using the HST (Hutchings et al. 1994, Boyce et al. 1998, Hooper et al. 1997) have made use of the synthetic PSFs produced by the TINYTIM software package (Krist 1998). This software is capable of reproducing the WFPC2 PSF through any of the on-board filters, seemingly removing the need to sacrifice valuable orbits observing the empirical PSF. However, the inability of the TINYTIM software to reproduce the scattered light halo associated with the WFPC2 PSF (Krist 1998) make these model PSFs unsuitable for the convolution of model quasars. This fact is illustrated in Fig 1 which shows a comparison between the high dynamic range empirical PSF used in our analysis and the equivalent TINYTIM model. It is

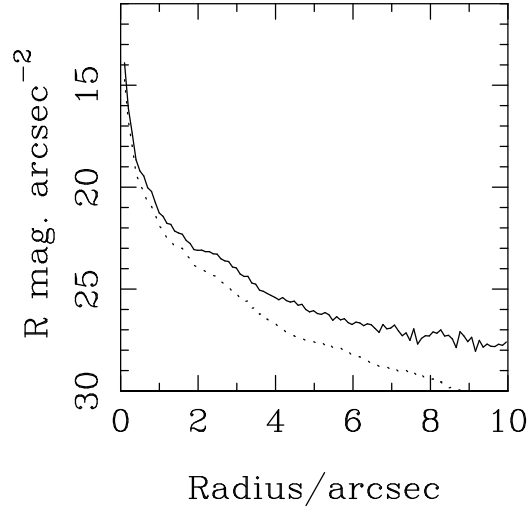


**Figure 1.** A comparison of our empirical F675W WF2 PSF (solid line) with the equivalent TINYTIM synthetic PSF (dashed line). Both have been normalized to have the same central surface-brightness. It can clearly be seen that the TINYTIM model is unable to reproduce the halo of scattered light outside a radius of  $\simeq 1.5''$ .

clear from this that if the model quasars do not include the scattered-light halo, the scalelengths of the underlying host galaxies could be seriously overestimated.

A further issue to be considered when analysing WFPC2 images is the severe undersampling of the WF CCDs. Given that the central  $1''$  of the *R*-band quasar images presented in McLure et al. (1999) and Dunlop et al. (2000) are dominated by the unresolved nuclear component, it was imperative that the undersampling issue was dealt with properly. In order to deal with this problem a solution was arrived at which, makes use of the sub-sampling capabilities of the TINYTIM software. Although inadequate as a substitute for the empirical PSF at large radii, the synthetic models produced by TINYTIM are an excellent match to the empirical PSF in the very central regions where the optical effects are well understood. The ability of TINYTIM to produce PSF models at fifty times higher resolution than the WF2 plate-scale was used to predict the appearance of the central nine pixels of the WF2 PSF with any possible sub-pixel centring. These predictions are then  $\chi^2$  matched to the core (central nine pixels) of the quasar image to give centroiding with theoretical accuracy of  $\pm 0.02$  pixels. Assuming that the TINYTIM model provides an accurate representation of the true PSF in the central  $\simeq 0.5''$ , it is then possible to correct the sampling of the central regions of the empirical PSF to the same sub-pixel centring as that of the quasar image.

### 2.2 Error Allocation

Regardless of the care with which model quasars are constructed, two-dimensional modelling will fail to produce accurate results if incorrect allocation of error weighting in the  $\chi^2$  test causes one area of the image to dominate the fit at

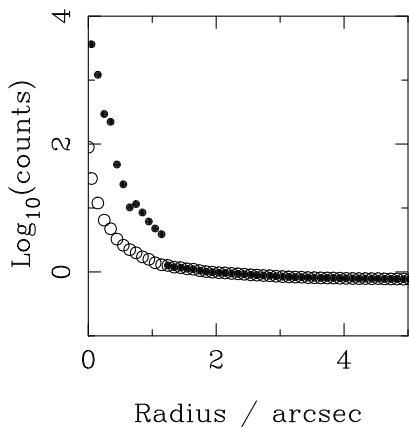


**Figure 2.** A typical HST error profile (0923+201). Shown in the figure are the predicted poisson errors (open circles) from the WF noise model, and the actual sampling errors (filled circles), both calculated from azimuthal averaging in circular annuli. It can be seen that outside a radius of  $\sim 1''$  the poisson and sampling errors are basically identical.

the expense of others. The minimum possible error that can be associated with any pixel is a combination of the poisson error due to photon shot noise, plus the read-noise and dark current contributions. Errors introduced during flat-fielding have proven to be negligible in both the HST data and the IRCAM 3 images considered in here. Figure 2 shows a comparison between poisson noise predicted by the WF2 noise model (Biretta et al. 1996), and the actual statistical sampling errors as measured from a typical image.

As can be seen from Fig 2, the errors calculated using the noise model are in near-perfect agreement with what is actually seen from the data for all pixels outside a radius of  $\simeq 1''$  from the quasar core. Consequently, all pixels outside a radius of  $1''$  are simply allocated their expected poisson error during the model fitting process. However, Fig 2 also demonstrates that this system would grossly underestimate the actual error introduced inside  $\simeq 1''$  by the severe undersampling of the WFPC2 PSF. Therefore, inside a radius of  $1''$  a different system is used to allocate the error weighting. A series of ten pixel-wide circular annuli centred on the quasar are constructed, and the variance ( $\sigma^2$ ) of the distribution of the pixels falling within each annuli calculated. All of the pixels falling within a particular annulus are then allocated the annulus variance as their error weighting. This procedure is still justified even when the underlying host galaxy has a clear ellipticity since, even at HST resolution, the central  $1''$  of the quasar images are dominated by the circular symmetry of the PSF. Due to the success of the re-sampling technique discussed above, it was possible to assign a poisson error weighting to the central pixel without biasing the fitting procedure. This complicated process has proven to be successful, with the vast majority of the 33 HST objects modelled having minimum  $\chi^2$  solutions lying in the  $\nu \pm \sqrt{2\nu}$  region expected for correct weighting (Dunlop et al. 2000). Confidence in the weighting system is further strengthened by examination of the pixel maps of reduced  $\chi^2$  values produced for the best-fitting models. Shown in Fig 3 a typical  $\chi^2$  map from the best-fit to the radio-loud quasar 1217+023. It is clear from this figure that the desired

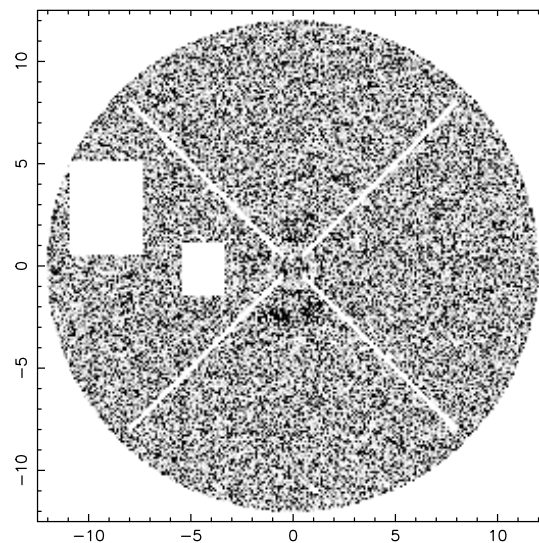


**Figure 3.** The reduced  $\chi^2$  map for the best-fitting model to the HST image of the radio-loud quasar 1217+023. The grey-scale is a linear stretch running between  $0 \rightarrow 2$ . It can be seen that a uniform spread of  $\chi^2$  values has been achieved, with no area of the image dominating the fit. The blank areas in the map are due to the masking from the fitting process of two companion objects and the highly variable diffraction spikes.

uniform spread of  $\chi^2$  values has been achieved, with no one area of the image dominating the fit.

### 2.3 Minimization

The main advantage of the two-dimensional modelling technique being adopted here is that it allows each individual pixel in the image frame to be included in the model fitting as a degree of freedom. However, due to the high angular resolution of our data, a typical model fit to a radius of  $12''$  will include some 45000 WFPC2 pixels ( $\sim 5700$  IRCAM3 pixels) in each  $\chi^2$  evaluation. The adopted solution was to utilise the downhill simplex method (Press et al. 1989) to locate the global minimum. Although significantly slower than the conjugate gradient method used in Taylor et al. (1996), downhill simplex minimization was chosen for its robustness in finding the true global minimum, and its insensitivity to the selection of initial conditions.

To determine the prevalence of false minima in the hyper-surface, a high-resolution grid search was undertaken for two objects, with the extent of the search grid being  $\pm 20\%$  from the parameter values found by the minimization routine. The results of the grid search for the radio galaxy 3C234.0, which contains a 30% nuclear component, are shown in Fig 4 with the position of the global minimum marked with  $\odot$ . Two features of this diagram are worthy of comment. Firstly it can be seen that in both parameter slices the minimum  $\chi^2$  value lies at the bottom of a narrow ‘valley’, suggesting that false minima are not ubiquitous. Secondly, despite the expected correlation between galaxy scalelength and central surface-brightness (Abraham et al. 1992), the minimization routine has still successfully located the global minimum.

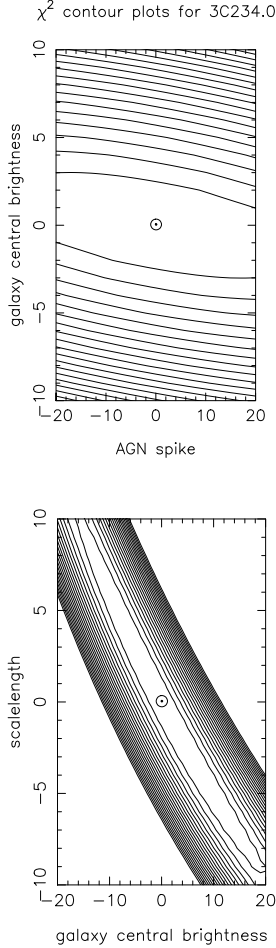


**Figure 4.**  $\chi^2$  contour maps for the radio galaxy 3C234.0 showing 2-parameter slices through the 5-parameter hypersurface. Contour levels are spaced at intervals of  $\Delta\chi^2 = 100$  from the minimum  $\chi^2$  (marked with  $\odot$ ).

### 3 TESTING THE MODELLING CODE

For the purposes of the full HST host galaxy study it was essential to determine the typical accuracy with which host-galaxy parameters could be recovered. Due to the nature of host galaxy work, a data-set for which the host galaxy parameters have been accurately determined previously does not exist, and consequently, an extensive programme of tests was undertaken using synthetic data.

To allow a realistic representation of the range of redshifts displayed by the WFPC2 data the synthetic AGN were constructed at three redshifts,  $z=0.1$ ,  $z=0.2$  &  $z=0.3$ . At each redshift 28 elliptical and 28 disc host galaxies models were constructed. Each group of 28 host galaxies consisted of a range of four possible half-light radii (5, 10, 15 and 20 kpc for  $\Omega_0 = 1.0, H_0 = 50$ ), all of which had the same integrated luminosity. To each of these four different galaxy scalelengths a range of seven possible nuclear components were added, giving  $L_{nuc}/L_{host}$  ratios in the range  $0 \rightarrow 16$ . The synthetic AGN with no nuclear component were included to check that the modelling code did not have a bias towards preferring a nuclear component where none existed. The final ensemble of models totalled 168 and covered the full range of parameters likely to occur in reality.

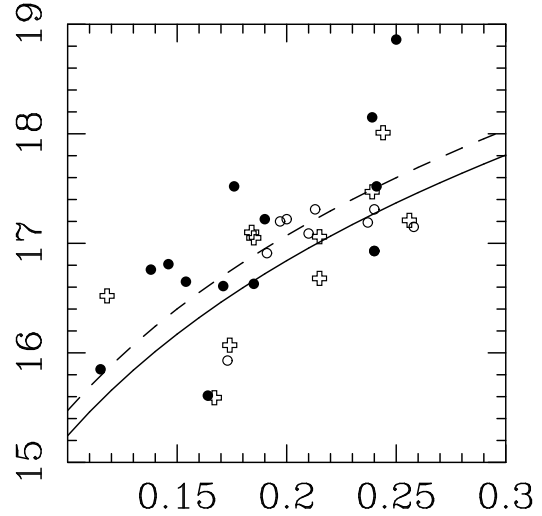


**Figure 5.** The apparent magnitude versus redshift distribution of the best-fitting host galaxies of the HST sample (Dunlop et al. 2000). Shown in the diagram are radio galaxies (crosses), radio-loud quasars (open circles) and radio-quiet quasars (filled circles). Also shown is the apparent magnitude of the synthetic host galaxies used for testing the two-dimensional modelling code (solid line). The dashed line shows the apparent magnitudes of the synthetic hosts dimmed by 0.27 magnitudes (see text).

### 3.1 Synthetic Quasar Construction

When constructing the suite of synthetic quasars several steps were taken to ensure that these simulations reflected the characteristics of actual WFPC2 observations as closely as possible. The first step was to construct the final synthetic quasar images from a stack of separate frames in an identical fashion to the real data. As described in McLure et al. (1999), the actual quasar observations consist of three deep 600-second exposures which were complimented by three shorter snap-shot exposures of 5, 26 and 40 seconds, designed to ensure a unsaturated measure of the nuclear component. The final reduced quasar images consist of a stack of the three long exposures, with the central regions replaced by a scaled snap-shot exposure to recover the quasar's full dynamic range. The construction of the synthetic quasars proceeded in exactly the same fashion, with individual simulations of each of the six separate exposures. An appropriate level of background counts were then added to each of the simulated exposures before they were processed by the IRAF routine MKNOISE which simulated the effects of both shot and read-out noise.

The fiducial luminosity of the simulated host galaxies was chosen to match the absolute magnitude of the best-fit to PKS 2247+14 ( $M_R = -23.8$ ), which was typical of the 12 hosts which had been observed at the time. The calculation of the absolute luminosity of the hosts at the three redshifts was then determined assuming a typical spectral index of  $\alpha = 1.5$  for the F675W filter ( $f_\nu \propto \nu^{-\alpha}$ ), and a cosmology with  $H_0 = 50 \text{ km s}^{-1} \text{ Mpc}^{-1}$  and  $\Omega_0 = 1$ . The cosmological dimming of the AGN point source assumed a spectral index of  $\alpha = 0.2$  (Neugebauer et al. 1987). Figure 5 shows the apparent magnitudes for all 33 host galaxies from the HST programme (see Dunlop et al. 2000) plotted against redshift.

Also shown are the apparent magnitudes of the synthetic host galaxies. There is a suggestion from Fig 5 that the synthetic galaxies are fractionally too bright compared to the data, making it arguably slightly too easy for the code to recover the galaxy parameters from the simulated images. This is confirmed by the results for the full sample which show the mean absolute luminosity of the 33 host galaxies to be  $M_R = -23.53$ , 0.27 magnitudes fainter than the synthetic hosts used in the testing programme. To illustrate this point the dashed line in Fig 5 shows the apparent magnitude of the synthetic host galaxies dimmed by a further 0.27 magnitudes, which clearly provides a better match to the data. However, the overestimate of the typical host luminosity should be more that off-set by the much larger range of  $L_{nuc}/L_{host}$  tackled by the modelling code during testing. While the average  $L_{nuc}/L_{host}$  of the quasars from the HST programme is only 2.6, the code has been tested with values of  $L_{nuc}/L_{host}$  in the range  $0 \rightarrow 16$ .

One final measure was taken to improve the realism of the synthetic quasar images. The empirical PSF which was used during the production of the synthetic data had an artificial centroiding shift of  $\simeq 0.01''$  applied to it, significantly greater than the estimated centroiding error. This precaution was taken in light of the fact that using the same PSF to convolve both the synthetic images and the models used in the fitting process is obviously an idealised situation.

The results from the modelling of the synthetic quasars are listed in Tables 1, 2 and 3. Two features of these results are worthy of individual comment. Firstly, it can be seen that for both host morphologies the errors associated with the determination of all the parameters steadily increase with redshift, as is expected due to inevitable drop in signal-to-noise. Secondly, with regards to the host scalelength it can be seen to be significantly easier to accurately determine this parameter for disc hosts than for ellipticals. This is again as is expected considering the different behaviour of the Freeman and de Vaucouleurs surface-brightness laws in the central  $\simeq 1''$ . The cusp-like nature of the  $r^{1/4}$  law at small radii inevitably leads to greater difficulty in decoupling the relative contributions of the host and nuclear components.

The results of the synthetic data testing can be summarized as follows:

- 100% success in host morphology discrimination.
- host flux determination  $\geq 95\%$  accurate in all cases.
- error in  $r_e \leq 15\%$  out to  $z = 0.3$  for ellipticals.
- error in  $r_0 \leq 3\%$  out to  $z = 0.3$  for discs.

where successful morphological determination refers to a  $\Delta\chi^2 \geq 25.7$  between the best-fitting model of the correct morphology, and the best-fitting alternative model, a difference equivalent to the 99.99% confidence level for a 5-parameter fit (Press et al. 1989). Although the high degree of accuracy achieved in these simulations is impressive, it should be noted that these error estimates are only valid for the high resolution data provided by HST. As will be seen in Section 6, the errors associated with ground-based data can be significantly larger.

| z   | $r_{1/2}$<br>/kpc | Nuc<br>Flux | $r_{1/2}$ | PA   | b/a  | Host<br>Flux | Nuc/Host<br>Ratio |
|-----|-------------------|-------------|-----------|------|------|--------------|-------------------|
| 0.1 | 5                 | 2.50        | 2.40      | 0.04 | 0.69 | 0.37         | 2.62              |
| 0.1 | 10                | 1.77        | 2.90      | 0.13 | 0.67 | 0.83         | 1.15              |
| 0.1 | 15                | 1.48        | 3.09      | 0.13 | 0.97 | 1.26         | 0.35              |
| 0.1 | 20                | 1.33        | 3.44      | 0.30 | 1.41 | 1.86         | 0.82              |
| 0.2 | 5                 | 2.15        | 5.17      | 0.71 | 1.33 | 0.90         | 2.67              |
| 0.2 | 10                | 2.52        | 6.17      | 1.02 | 1.84 | 1.21         | 1.47              |
| 0.2 | 15                | 2.25        | 6.86      | 0.59 | 2.20 | 2.59         | 0.80              |
| 0.2 | 20                | 1.78        | 7.51      | 0.46 | 2.77 | 3.76         | 2.03              |
| 0.3 | 5                 | 2.48        | 8.91      | 1.51 | 1.63 | 1.83         | 1.73              |
| 0.3 | 10                | 3.10        | 9.59      | 1.63 | 2.96 | 1.54         | 1.43              |
| 0.3 | 15                | 2.42        | 10.3      | 1.13 | 2.54 | 3.73         | 1.48              |
| 0.3 | 20                | 1.18        | 9.43      | 2.31 | 3.31 | 4.84         | 2.29              |

**Table 1.** Results of the two-dimensional modelling tests using synthetic quasars with elliptical host galaxies. Column 1 gives the redshift of the quasar. Column 2 gives the actual scalelength of the simulated host in kpc. Columns 3-8 give the mean percentage error in the reclaimed value of the relevant parameter. Each value is the mean for the seven synthetic quasars produced at a particular redshift, with a particular scalelength (for each redshift and scalelength combination there where seven different synthetic quasars produced with  $L_{nuc}/L_{host}=0, 0.5, 1.0, 2.0, 4.0, 8.0$  & 16).

| z   | $r_{1/2}$<br>/kpc | Nuc<br>Flux | $r_{1/2}$ | PA   | b/a  | Host<br>Flux | Nuc/Host<br>Ratio |
|-----|-------------------|-------------|-----------|------|------|--------------|-------------------|
| 0.1 | 5                 | 1.10        | 0.53      | 0.11 | 0.23 | 0.16         | 1.30              |
| 0.1 | 10                | 0.27        | 0.44      | 0.30 | 0.89 | 0.73         | 0.48              |
| 0.1 | 15                | 0.13        | 0.43      | 0.34 | 1.64 | 1.10         | 1.22              |
| 0.1 | 20                | 0.13        | 0.70      | 0.66 | 2.51 | 1.43         | 1.40              |
| 0.2 | 5                 | 1.60        | 1.07      | 0.43 | 0.80 | 0.57         | 1.83              |
| 0.2 | 10                | 1.32        | 1.36      | 0.69 | 1.97 | 1.07         | 1.13              |
| 0.2 | 15                | 0.48        | 1.23      | 0.67 | 3.16 | 2.01         | 2.12              |
| 0.2 | 20                | 0.48        | 1.67      | 0.65 | 5.39 | 2.79         | 2.60              |
| 0.3 | 5                 | 1.53        | 1.37      | 0.67 | 0.56 | 0.74         | 1.73              |
| 0.3 | 10                | 1.90        | 1.97      | 1.47 | 2.77 | 1.74         | 0.75              |
| 0.3 | 15                | 0.42        | 1.87      | 1.20 | 4.27 | 2.17         | 2.10              |
| 0.3 | 20                | 0.33        | 1.76      | 2.11 | 4.96 | 2.50         | 2.67              |

**Table 2.** Results of the two-dimensional modelling tests using synthetic quasars with disc host galaxies. Columns as Table 1.

#### 4 BETA PARAMETER MODELLING

Due to the success of the programme of tests outlined above, it was felt that the level of information present in the HST data justified an extension of the modelling code to cover more than just fixed elliptical and disc host galaxies. The modelling code as described so far is able to determine host galaxy morphology only to the extent that it is elliptical-like or disc-like. Given that the results of the synthetic quasar testing show that it is relatively easy to discriminate between idealised elliptical and disc host galaxies, it is interesting to ask whether it is also possible to quantify just how similar the host galaxy surface-brightness distributions are to the classical  $r^{1/4}$  or exponential laws. This question has particular relevance because of recent studies of the cores of inactive elliptical galaxies using both HST (Lauer et al. 1995) and ground-based imaging (D’Onofrio *et al.* 1994)

| Host Type  | $z$ | $r_{1/2}$ | PA      | b/a     | Host Flux (12'') | Nuc/Host Ratio |
|------------|-----|-----------|---------|---------|------------------|----------------|
| disc       | 0.1 | 0.2→1.3   | 0.0→2.3 | 0.8→5.4 | 0.1→5.0          | 0.0→4.5        |
| elliptical | 0.1 | 1.6→4.8   | 0.0→0.6 | 0.0→2.3 | 0.1→2.3          | 0.0→4.0        |
| disc       | 0.2 | 0.8→1.9   | 0.0→2.3 | 0.8→5.4 | 0.1→2.5          | 0.0→4.5        |
| elliptical | 0.2 | 2.4→11.5  | 0.0→1.7 | 0.8→3.1 | 0.2→4.3          | 0.0→4.5        |
| disc       | 0.3 | 0.0→2.6   | 0.0→3.7 | 0.0→5.4 | 0.1→3.0          | 0.0→4.0        |
| elliptical | 0.3 | 6.0→13.7  | 0.0→6.3 | 0.8→4.6 | 0.2→5.0          | 0.0→6.8        |

**Table 3.** The range of percentage errors in the reclaimed values of the host-galaxy parameters from the synthetic quasar modelling tests. Columns 1 & 2 detail the actual host-galaxy morphology and redshift of the synthetic quasars. Columns 3 → 7 show the range in percentage error in the reclaimed parameters from the model fits to the 28 synthetic quasars constructed at each redshift, with each of the two host morphologies.

which suggest that the surface-brightness profiles of these galaxies can deviate significantly from an  $r^{1/4}$  law. It is also of some interest to determine whether or not the code can differentiate between the  $r^{1/4}$  law and a somewhat flatter relation at ( $r \geq r_e$ ) given the substantial evidence that brightest cluster galaxies (BCG) display so-called ‘halos’ in their surface-brightness distributions at large radii (Graham et al. 1996, Schombert 1987).

The Freeman exponential law and the de Vaucouleurs  $r^{1/4}$  law can be thought of as special cases of a more general form of surface-brightness distribution:

$$\mu(r) = \mu_o \exp\left(-\left(\frac{r}{r_o}\right)^\beta\right) \quad (3)$$

where the form of the radial profile is governed by the extra free parameter  $\beta$  (Sersic 1968). A further batch of testing was undertaken to determine whether the value of this  $\beta$  parameter could be recovered with useful accuracy.

#### 4.1 Testing the Beta Modelling Code

The question which was asked of the  $\beta$ -modelling code was whether, given a sample of synthetic quasars with idealised de Vaucouleurs host galaxies, could it return a range of  $\beta$  values narrow enough to provide useful extra information. The accuracy of the  $\beta$ -modelling code was tested using the 56  $z = 0.2$  &  $z = 0.3$  synthetic quasars with elliptical hosts from Section 3. It was not considered necessary to test the  $\beta$ -modelling code using idealised Freeman disc hosts since the test results presented in Section 3 showed that it is substantially more difficult to recover the parameters of elliptical hosts in all cases. The success of the  $\beta$ -modelling code can be immediately seen from Fig 6. Out of the 56 synthetic quasars tested, the  $\beta$  value recovered by the modelling code lies in the range  $0.225 < \beta < 0.275$  in 53 cases.

## 5 COMBINED DISK-BULGE MODELLING

During the latter stages of the analysis of the HST host galaxies presented by Dunlop et al. (2000), it became necessary to extend the modelling code further than has been described above. The  $\beta$ -modelling of four of the radio-quiet quasars from the the HST sample showed that the underlying host galaxy was a hybrid of both disk and bulge (elliptical) forms. To investigate whether an improved fit could be achieved

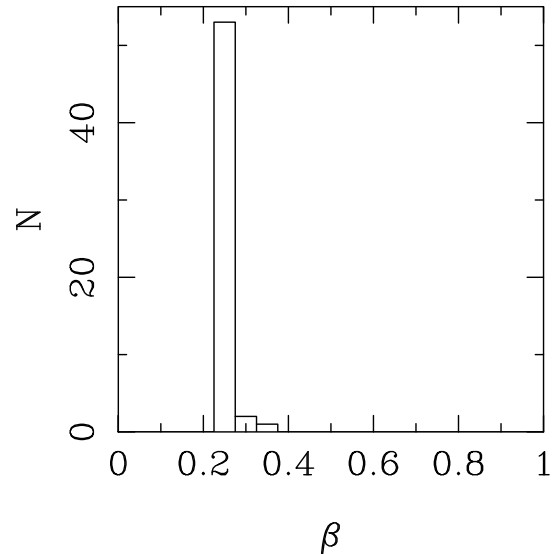


**Figure 6.** The distribution of beta values recovered by the  $\beta$ -modelling code from the synthetic quasars with elliptical host galaxies at  $z=0.2$  and  $z=0.3$ .

with a two-component model the central model-building algorithm was extended to produce combined disk and bulge models. During the fitting of these combined models the eight parameters controlling the form of the galaxy surface-brightness distributions were left free. In combination with the normalization of the nuclear component this required the fitting of a total of nine free parameters.

With regards to host-galaxy morphology, the clear conclusion from both sets of modelling tests presented here is that if the host galaxies of the AGN in the HST imaging study are consistent with standard de Vaucouleurs or Freeman models, then the two-dimensional modelling code will successfully discriminate between the two. In addition to this, if the distribution of  $\beta$  values returned from the modelling of the host galaxies does not show a strong peak around either  $\beta = 0.25$  or  $\beta = 1.0$ , then this can be taken as strong evidence the host galaxies deviate significantly from the simple elliptical and disc forms, either because they contain a significant mix of bulge and disc components, or, for example, because they have been distorted by gravitational interaction with a companion.

## 6 TIP-TILT OBSERVATIONS OF QUASAR HOST GALAXIES

With the arrival of active and adaptive optics systems the prospect of near diffraction-limited ground-based imaging has become a reality. Within the context of the study of quasar host galaxies this development perhaps has most relevance in the near-infrared. The inherent advantages of observing host galaxies in the near-infrared were discussed by Dunlop et al. (1993), and formed the motivation for the original IRCAM 1  $K$ -band imaging of the HST sample (Dunlop et al. 1993; Taylor et al. 1996). The main limitation of the existing  $K$ -band imaging of this sample is the inability to reliably distinguish the host galaxy morphology in quasars where the  $L_{nuc}/L_{host} \geq 5$  due to the ground-based seeing of  $\geq 1''$ . In this section the results are presented from a short observing run which was designed to explore whether the sub-arcsec imaging quality now readily attainable with tip-tilt active optics at UKIRT could rectify this problem.

### 6.1 The Sample

The observed sample consists of 9 objects (Table 4) which were chosen to fully quantify the improvements that could be gained over the previous  $K$ -band imaging study. Six of the quasars were taken from the original 40-object sample described in Taylor et al. (1996), with five of these also featuring in the new HST sample. The remaining three objects were taken from the sample of Bahcall et al. (1994), and were selected because of the original failure to detect a host galaxy from  $V$ -band HST imaging (Bahcall et al. 1994, 1995a). Four of the six objects taken from the original 40-object sample (marked with a  $\star$  in Table 4) were specifically chosen for this project because the modelling of the original IRCAM1 observations was unable to determine the host morphology due to their high  $L_{nuc}/L_{host}$ . These objects presented an ideal opportunity to investigate the advantages to be gained by confining the nuclear flux to within the central  $0.5 \rightarrow 1''$  with active optics. The remaining two objects, on the contrary, were specifically chosen because the model fits from the previous analysis were regarded as secure, with a strong preference being shown for one particular host morphology.

### 6.2 The Observations

The new  $K$ -band observations were made on 5-7th April 1997 using the IRCAM 3 infrared camera on the 3.9m United Kingdom Infrared Telescope (UKIRT) on Mauna Kea, Hawaii. IRCAM 3 is a  $256 \times 256$  InSb array which was operated in  $0.281 \text{ arcsec pixel}^{-1}$  mode, providing a field-of-view of approximately  $70''$ . The observing run for this project was among the first ever to make full use of the tip-tilt active optics system, producing images with consistent resolution of  $\simeq 0.7''$ . The following observational procedure was used.

Each object was observed using a 4-point jitter pattern with each point consisting of 3 minutes of integration broken into 18 co-adds of 10-seconds duration. This combination was chosen specifically in order to provide unsaturated but background-limited images. This 12-minute jitter pattern was repeated six times for each object, providing a total

| Source           | Type | $z$   | $V$  | Time (mins) | Comment |
|------------------|------|-------|------|-------------|---------|
| 0923+201 $\star$ | RQQ  | 0.190 | 15.8 | 72          | Good    |
| 0953+415 $\star$ | RQQ  | 0.239 | 15.6 | 72          | Good    |
| 1004+130 $\star$ | RLQ  | 0.240 | 15.2 | 72          | Good    |
| 1217+023         | RLQ  | 0.240 | 16.5 | 72          | Good    |
| 1012+008         | RQQ  | 0.185 | 15.9 | 72          | EN      |
| 1048-090 $\star$ | RLQ  | 0.345 | 17.0 | 72          | PD      |
| 1202+281         | RQQ  | 0.165 | 15.6 | 36          | Low SNR |
| 1302-102         | RLQ  | 0.286 | 15.2 | 72          | PD      |
| 1307+085         | RQQ  | 0.155 | 15.1 | 72          | Cloud   |

**Table 4.** The sample. The first six objects listed are taken from the original  $K$ -band imaging sample (Taylor et al. 1996). The final three objects have been taken from the sample imaged by Bahcall et al. (1994). Column five lists the on-source integration time for each object. Column six details any problems experienced with the images: EN = Electronic Noise, PD = Pointing Drift. Redshifts and  $V$  magnitudes have been taken from Taylor et al. (1996) and Bahcall et al. (1997) respectively.

of 72 minutes of on-source integration. Considering the desirability in host galaxy observations of confining the quasar nuclear flux to as small an angular extent as possible, the quasar nucleus itself was used as the tip-tilt guide-star in an attempt to obtain the best possible resolution. In order to provide high signal-to-noise measurements of the IRCAM 3 PSF, and to calibrate our photometry, observations of standard stars were taken before and after the completion of each jitter pattern.

### 6.3 Reduction

Following dark-frame subtraction each object was flat-fielded using concurrent sky flat-fields produced by a process of median filtering of the 24 individual 3-minute integrations. Due to the considerable angular extent of the host galaxies ( $\simeq 15''$ ) compared with the IRCAM 3 field-of-view, this median filtering had to be performed on a quadrant-by-quadrant basis. As a result of the jitter pattern, each quadrant of the array looked at blank sky for 3/4 of the total integration time for each object. These frames could be median filtered without fear of contamination from host galaxy light. The four flat-field quadrants produced in this fashion were then added together and normalized to unit median to produce the final flat-field. After flat-fielding the individual 3-minute frames were corrected for the known non-linearity of the IRCAM 3 detector before being re-registered and stacked to produce the final deep images for analysis.

### 6.4 Image Defects

Several problems with the data obtained during this observing run limited the number of objects which could be successfully analysed with the modelling code. Firstly, the two highest redshift objects (1048-090 & 1302-102) proved to have nuclear luminosities which were insufficient to provide stable pointing with the tip-tilt system. The consequent wandering of the telescope pointing during the observations of these two objects resulted in final mosaiced images from

which it was impossible to accurately separate the host and nuclear light. Secondly, all of the images obtained were affected to some extent by bands of spurious electronic noise, with 1012+008 being the source worst effected. It proved impossible to construct a reliable flat-field for this object, and it is was therefore dropped from the modelling process.

The data for two more of the nine objects listed in Table 4 were of insufficient quality to successfully model the underlying host galaxies. In the case of 1202+281 this was simply due to the integration time acquired (36 minutes) providing low signal-to-noise, while 1307+085 was rejected due to flat-fielding problems produced by partial cloud-cover.

The result of these technical difficulties was that only four objects yielded data of the high quality required by the two-dimensional modelling code. However, the remaining four objects still allowed the main objectives of the run to be achieved. Three of the objects were allocated unreliable fits from the previous *K*-band imaging, and therefore presented a good test of the improvements to be gained from the increased resolution of tip-tilt imaging. In addition to this, the final object (1217+023), was considered to have a reliable model fit and therefore gave an opportunity to see if the modelling of the new data was consistent with the previously obtained results.

### 6.5 The IRCAM3 Point Spread Function

As was mentioned in Section 6.2, standard stars were observed throughout the observations of each object to provide accurate, concurrent measures of the PSF. However, considering that the final deep quasar images are typically stacks of 24 individual 3-minute frames, in some cases taken over two nights, there is no guarantee that any one of the PSF observations will be a good match to the final mosaic. In an effort to overcome this problem, further tip-tilt PSF observations were included from a more recent UKIRT observing run (Percival et al. 2000), producing a library of 65 high signal-to-noise PSF observations. The following procedure was adopted for choosing the best PSF match for each quasar.

The central nine pixels ( $\simeq 0.5''$ ) of the quasar image was compared with each PSF via the  $\chi^2$  statistic. The five individual PSFs which provided the best match to the quasar core were then stacked to produce a composite PSF. The minimization routine described in Section 2.3 was then used to find the optimal weighting of the individual PSFs to produce the minimum  $\chi^2$  between the quasar core and the composite PSF.

### 6.6 Results

The results from the two-dimensional modelling of the four quasars which did not suffer from image degradation are listed in Table 5. Surface-brightness profiles extracted from the two-dimensional model fits are shown in Fig 8. Also shown in Table 6 are the results from the modelling of the HST *R*-band imaging of the four objects. These results are identical to those presented in McLure et al. (1999) and Dunlop et al. (2000), and are repeated here simply for ease of comparison with the new *K*-band results.

| Source   | $\Delta\chi^2$ | $r_e$ / kpc | $K_{host}$ | $K_{nuc}$ | b/a  | $L_n/L_h$ |
|----------|----------------|-------------|------------|-----------|------|-----------|
| 0923+201 | 27             | 8.6         | 13.98      | 12.48     | 0.87 | 3.98      |
| 0953+415 | 14             | 8.4         | 15.18      | 12.72     | 0.73 | 9.62      |
| 1004+130 | 276            | 8.5         | 13.92      | 12.90     | 0.85 | 2.55      |
| 1217+023 | 187            | 7.7         | 14.13      | 13.62     | 0.84 | 1.59      |

**Table 5.** Results of the two-dimensional modelling of the IRCAM 3 data. Column 2 lists the difference in  $\chi^2$  between the best elliptical and disc host galaxy fits (all sources were better described by an  $r^{1/4}$  fit). Column 3 details the effective radius of the best-fit host galaxy. Columns 4 & 5 list the integrated apparent magnitudes of the host and nuclear component respectively. Column 6 gives the axial ratio (*b/a*) for the best-fit host. Column 7 converts the figures of columns 4 & 5 into a nuclear:host ratio.

| Source   | $\Delta\chi^2$ | $r_e$ / kpc | $R_{host}$ | $R_{nuc}$ | b/a  | $L_n/L_h$ |
|----------|----------------|-------------|------------|-----------|------|-----------|
| 0923+201 | 1733           | 8.2         | 17.22      | 15.66     | 0.98 | 4.23      |
| 0953+415 | 91             | 7.1         | 18.15      | 15.19     | 0.86 | 15.39     |
| 1004+130 | 501            | 8.2         | 16.93      | 15.02     | 0.94 | 5.78      |
| 1217+023 | 2359           | 9.9         | 17.31      | 16.32     | 0.80 | 2.49      |

**Table 6.** Results of the two-dimensional modelling of the HST data. Columns are as Table 5 with the exception of columns 4 & 5 which here list the *R*-band magnitudes of the host and nuclear component respectively.

### 6.7 Host Morphologies

All four of the quasars are found to lie in elliptical host galaxies, just as they were from the HST imaging, despite 0923+201 and 0953+415 being radio-quiet. The morphological decision for 0953+415 is the least clear-cut, formally only  $2\sigma$ , as expected considering that it has by far the largest value of  $L_{nuc}/L_{host}$ . As well as being in agreement with the HST modelling results, the morphology decisions for the new *K*-band images of 0953+415 and 0923+201 are fully consistent with the predictions of Taylor et al. (1996) that luminous RQQs are likely to have early-type host galaxies, with 0953+415 and 0923+201 being the most optically luminous RQQs in the full HST sample.

### 6.8 Scalelengths

An investigation of Tables 5 and 6 shows that the best-fit scalelengths from the two independent sets of data are in excellent agreement. In both wavebands the hosts are found to have large, and very similar scalelengths, spanning a range of less than 3 kpc.

The general result that these quasars are hosted by large galaxies with scalelengths of  $r_e \simeq 10$  kpc is consistent with the conclusions of Taylor et al. (1996). However, with the exception of 0953+415, the scalelength results presented here are not in good agreement on an individual object-by-object basis, differing by more than a factor of two in all cases. The reason for this most likely lies in the fact that, again with the exception of 0953+415, the best-fitting  $L_{nuc}/L_{host}$  from the modelling of the IRCAM 1 data are  $2 \rightarrow 4$  times greater than those found using IRCAM 3. Given that an overestimate of the unresolved nuclear component will artificially lower the central surface-brightness of the best-fitting host-



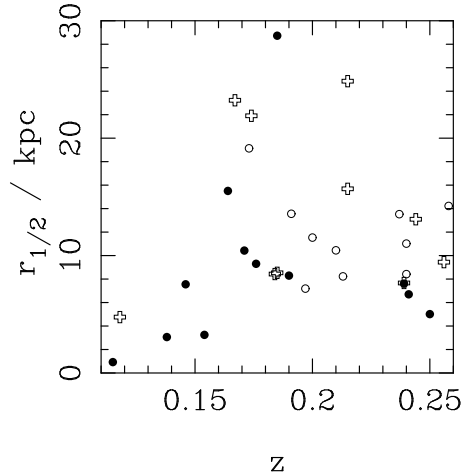


**Figure 7.** The  $r_{1/2}-z$  distribution of the best-fitting host models of the RG (crosses), RQQ (filled circles) and RLQ (open circles) sub-samples.

galaxy model, the requirement to match the host-galaxy flux at large radii will therefore lead to an inevitable overestimate of the host-galaxy scalelength. This conclusion is strengthened by a comparison of the HST scalelength results with the corresponding figures from Taylor et al. for all 33-objects in the HST sample (Dunlop et al. 2000). In the majority of cases there is a consistent bias in the previous IRCAM 1  $K$ -band modelling towards finding larger galaxies with a lower central surface-brightness, although the difference is generally not as great as that found for the four quasars presented here, which are amongst the most luminous in the sample. The detection of this bias confirms that scalelength values derived from data without sub-arcsec resolution should be regarded with some caution.

If viewed in isolation it could appear of some concern that the best-fit scalelengths of all four host galaxies should be so similar, given that three of them have identical redshifts. However, the possibility that there is some bias in the modelling can be firmly rejected for a number of reasons. Firstly, during the testing of the modelling code (Section 3) there was no such bias detected, with the code successfully discriminating between scalelengths in the range  $5 \rightarrow 20$  kpc. Secondly, the close agreement between the optical and infrared scalelengths derived for these four objects provides further reassurance that there is no correlation between scalelength and redshift, given that Fig 7 shows that no such correlation exists in the scalelengths determined for the full HST sample (Spearman rank test probability of  $p = 0.52$ ).

## 6.9 Host Luminosities and Colours

The integrated absolute  $K$ -band and  $R$ -band magnitudes of the best-fitting host galaxy models are presented in Table 7. The absolute magnitudes have been calculated using  $k$ -corrections assuming a spectral index  $\alpha = 0.0$  and  $\alpha = 1.5$  for the  $K$ - and  $R$ -band respectively ( $f_\nu \propto \nu^{-\alpha}$ ). The calculation of the host luminosities in terms of  $L^*$  have been performed taking  $M_K^* = -24.6$  (Gardner et al. 1997) and  $M_R^* = -22.3$  (calculated by converting the value of  $M_R^* = -21.8$  (Lin et al. 1996) to an integrated magnitude).

| Source   | $M_K$  | $L/L_K^*$ | $M_R$  | $L/L_R^*$ | $R-K$ |
|----------|--------|-----------|--------|-----------|-------|
| 0923+201 | -26.21 | 4.3       | -23.25 | 2.4       | 3.0   |
| 0953+415 | -25.48 | 2.2       | -22.82 | 1.6       | 2.7   |
| 1004+130 | -26.75 | 7.1       | -24.10 | 5.2       | 2.7   |
| 1217+023 | -26.54 | 5.9       | -23.71 | 3.7       | 2.8   |

**Table 7.** Luminosities and colours for the four best-fitting host galaxies. Column 2 lists the absolute integrated  $K$ -band magnitudes. Column 3 restates the absolute magnitudes in term of  $L^*$ . Columns 4 & 5 give the equivalent figures from the  $R$ -band HST modelling. Column 6 gives the resulting  $R-K$  colour for the host galaxies.

Again it can be seen that these results confirm the findings of the HST  $R$ -band imaging, and the previous  $K$ -band imaging (Taylor et al. 1996), that the quasar hosts are all luminous galaxies with  $L \geq 2L^*$ . The fact that in this small group of objects the RLQs are substantially more luminous than the RQQs should not be taken as significant since, 1004+130 and 1217+023 are found to be brighter than average for RLQs from the  $R$ -band modelling, while 0953+415 has the largest  $L_{nuc}/L_{host}$  ratio in the entire 33-object sample.

The excellent agreement of the model results from the  $K$ - and  $R$ -band imaging in terms of host morphology and scalelength allows an accurate measurement of the host galaxy optical-infrared colour to be made. The integrated, rest-frame,  $R-K$  colours listed in Table 7 can be seen to be perfectly consistent with that expected from an old passively evolving stellar population formed at  $z \geq 3$ . This conclusion is confirmed by the  $R-K$  colours of the full 33-object sample, where comparison with spectral synthesis models indicates that none of the AGN host galaxies have stellar populations younger than  $\sim 7$  Gyr at  $z=0.2$  (Dunlop et al. 2000). A further conclusion which can be drawn from the red colours of these host galaxies is that any star formation associated with the AGN activity must be confined to the central few kpc, and not widely distributed throughout the body of the host galaxy.

## 7 CONCLUSIONS

The results of applying our two-dimensional modelling technique to the full range of simulated quasar images provides confidence that, at least at  $z \simeq 0.1 - 0.3$  all derived host galaxy parameters can be trusted to a typical accuracy of better than 10%. This is perhaps not surprising for parameters such as host luminosity, position angle, and axial ratio, but accurate scalelength determination has proved particularly difficult in virtually all previous studies of quasar hosts. The reliability of our derived scalelengths is further reinforced by the virtually identical values yielded by the analysis of the infrared tip-tilt images discussed in the previous section. Indeed the fact that such similar scalelengths have resulted from analysis of images taken at different wavelengths, with different plate-scales, and using very different telescopes with very different PSF complications is undeniably impressive. It is this accuracy of scalelength determination that has enabled us, for the first time, to demonstrate that the hosts of RQQs, RLQs and RGs follow a Kormendy

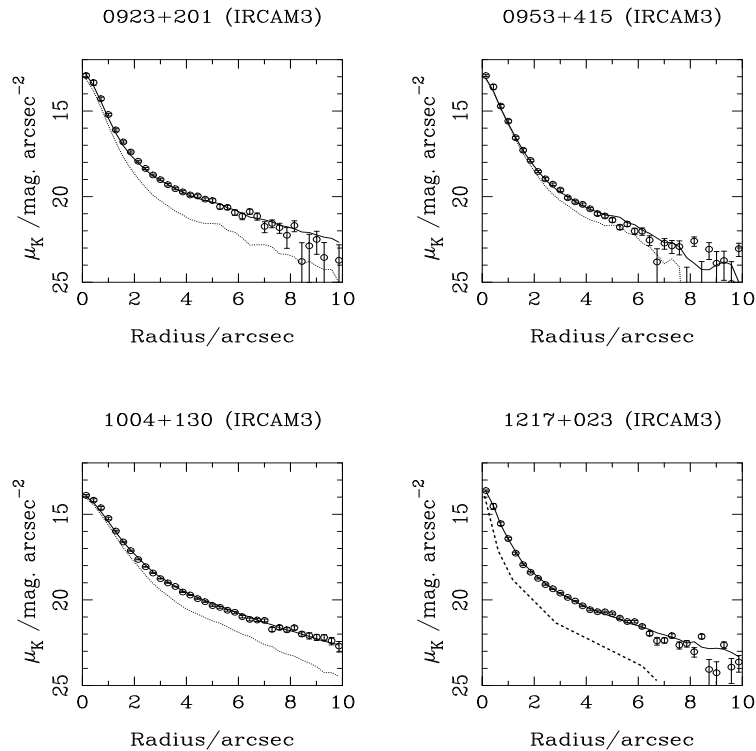


**Figure 8.** The surface-brightness profiles resulting from the two-dimensional modelling of the IRCAM3 data. Shown in the figure are the data (open circles), the best-fit model (solid line) and the best-fit nuclear component (dashed line).

relation with slope and normalization identical to that displayed by ‘normal’ low-redshift massive ellipticals (McLure et al. 1999; Dunlop et al. 2000).

The analysis of the new, higher-resolution (cf Dunlop et al. 1993) infrared images of the 4 quasars imaged with IRCAM3 indicates that galaxy scalelength is (perhaps unsurprisingly) essentially unchanged between the  $R$  and  $K$  wavebands, and that the HST-derived scalelengths should be trusted in preference to those derived by Taylor et al. (1996) from the IRCAM1 images of Dunlop et al. (1993). In at least some cases the original infrared-based host-galaxy scalelengths appear to have been over-estimated from the IRCAM1 images, although not sufficiently to alter the basic conclusions of Taylor et al. (1996). This has been taken into account in a re-analysis of the IRCAM1 data undertaken by Dunlop et al. (2000) in order to derive reliable  $R-K$  colours for *all* the host galaxies in the HST sample.

## 8 ACKNOWLEDGEMENTS

We thank the referee for comments which improved a number of aspects of this paper. The United Kingdom Infrared Telescope is operated by the Joint Astronomy Centre on behalf of the U.K. Particle Physics and Astronomy Research Council. Based on observations with the NASA/ESA Hubble Space Telescope, obtained at the Space Telescope Science Institute, which is operated by the Association of Universities for Research in Astronomy, Inc. under NASA contract No. NAS5-26555. This research has made use of the NASA/IPAC Extragalactic Database (NED) which is operated by the Jet Propulsion Laboratory, California Institute

of Technology, under contract with the National Aeronautics and Space Administration. MJK acknowledges the award of a PPARC PDRA, and also acknowledges support for this work provided by NASA through grant numbers O0548 and O0573 from the Space Telescope Science Institute, which is operated by AURA, Inc., under NASA contract NAS5-26555. RJM acknowledges a PPARC studentship.

## 9 REFERENCES

- Abraham R.G., Crawford C.S., McHardy I.M., 1992, ApJ, 401, 474
- Bahcall J.N., Kirhakos S., Schneider D.P., 1994, ApJ, 435, L11
- Bahcall J.N., Kirhakos S., Schneider D.P., 1995a, ApJ, 447, L1
- Biretta J.A., et al., 1996, WFPC2 Instrument Handbook Version 4.0
- Boyce P.J., et al., 1998, MNRAS, 298, 121
- De Vaucouleurs G., Capaccioli M., 1978, ApJS, 40, 699
- D’Onofrio M., Capaccioli M., Caon N., 1994, MNRAS, 271, 523
- Dunlop J.S., Taylor G.L., Hughes D.H., Robson E.I., 1993, MNRAS, 264, 455
- Dunlop J.S., McLure R.J., Kukula M.J., Baum S.A., O’Dea C.P., 2000, MNRAS, submitted
- Freeman K.C., 1970, ApJ, 160, 811
- Gardner J.P., Sharples R.M., Frenk C.S., Carrasco B.E., 1997, A&AS, 190, 4303
- Graham A., Lauer T.R., Colless M., Postman M., 1996, ApJ, 465, 534

- Hooper E.J., Impey C.D., Foltz C.B., 1997, *ApJ*, 480, L95  
Hutchings J.B., Morris S.C., Gower A.C., Lester M.L., 1994, *ApJ*, 429, L1  
Krist J., 1998, *TinyTim User Manual*  
Lauer T.R., et al., 1995, *AJ*, 110, 2622  
Lin H., Krishna R.P., Shethman S.A., Landy S.D., Oemler A., Tucker D.L., Schechter P.L., 1996, *ApJ*, 464, 60  
McLure R.J., Kukula M.J., Dunlop J.S., Baum S.A., O’Dea C.P., Hughes D.H., 1999, *MNRAS*, 308, 377  
Neugebauer G., Green G.F., Matthews K., McGill J., Scoville N., Soifer B.T., 1987, *ApJS*, 93, 1057  
Percival W., Miller L., McLure R.J., Dunlop J.S., 2000, *MNRAS*, astro-ph/0002199  
Press W.H., 1989, “*Numerical Recipes*”, Cambridge University Press  
Schombert J.M., 1987, *ApJS*, 64, 643  
Sersic J.L., 1968, *Atlas de Galaxies australes*. Observatorio Astronomico Cordoba  
Taylor G.T., Dunlop J.S., Hughes D.H., Robson E.I., 1996, *MNRAS*, 283, 930